Geoscience Frontiers xxx (2018) 1–9

HOSTED BY

ELSEVIER

Contents lists available at ScienceDirect

China University of Geosciences (Beijing)

Geoscience Frontiers

journal homepage: www.elsevier.com/locate/gsf

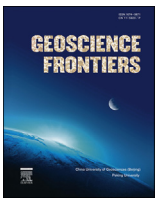

Research Paper

Time-resolved, defect-hosted, trace element mobility in deformed Witwatersrand pyrite

Denis Fougerouse [a,b,*], Steven M. Reddy [a,b], Christopher L. Kirkland [a], David W. Saxey [b], William D. Rickard [b], Robert M. Hough [c]

[a] School of Earth and Planetary Sciences, The Institute for Geoscience Research (TIGeR), Curtin University, GPO Box U1987, Perth, WA, 6845, Australia
[b] Geoscience Atom Probe, Advanced Resource Characterisation Facility, John de Laeter Centre, Curtin University, GPO Box U1987, Perth, WA, 6845, Australia
[c] CSIRO Minerals Resources, Kensington, WA, Australia

ARTICLE INFO

Article history:
Received 8 December 2017
Received in revised form
16 March 2018
Accepted 28 March 2018
Available online xxx

Keywords:
Atom probe microscopy
Nanoscale
Nanogeochronology
Microstructure
Isotope geochemistry
Common Pb

ABSTRACT

The Pb isotopic composition of rocks is widely used to constrain the sources and mobility of melts and hydrothermal fluids in the Earth's crust. In many cases, the Pb isotopic composition appears to represent mixing of multiple Pb reservoirs. However, the nature, scale and mechanisms responsible for isotopic mixing are not well known. Additionally, the trace element composition of sulphide minerals are routinely used in ore deposit research, mineral exploration and environmental studies, though little is known about element mobility in sulphides during metamorphism and deformation. To investigate the mechanisms of trace element mobility in a deformed Witwatersrand pyrite (FeS_2), we have combined electron backscatter diffraction (EBSD) and atom probe microscopy (APM). The results indicate that the pyrite microstructural features record widely different Pb isotopic compositions, covering the entire range of previously published sulphide Pb compositions from the Witwatersrand basin. We show that entangled dislocations record enhanced Pb, Sb, Ni, Tl and Cu composition likely due to entrapment and short-circuit diffusion in dislocation cores. These dislocations preserve the Pb isotopic composition of the pyrite at the time of growth (~3 Ga) and show that dislocation intersections, likely to be common in deforming minerals, limit trace element mobility. In contrast, Pb, As, Ni, Co, Sb and Bi decorate a high-angle grain boundary which formed soon after crystallisation by sub-grain rotation recrystallization. Pb isotopic composition within this boundary indicates the addition of externally-derived Pb and trace elements during greenschist metamorphism at ~2 Ga. Our results show that discrete Pb reservoirs are nanometric in scale, and illustrate that grain boundaries may remain open systems for trace element mobility over 1 billion years after their formation.

1. Introduction

Mineral deformation by crystal plasticity produces microstructures (e.g. dislocations, low- and high-angle boundaries) which can be compositionally different from the host mineral at the micrometre to nanometre scale (Lee, 1995; Ando et al., 2001; Büttner and Kasemann, 2007; McCaig et al., 2007; Nakagawa et al., 2011; Fougerouse et al., 2016a). Several non-exclusive mechanisms can be responsible for element mobility depending on the physico-chemical properties of the crystalline system and its environment. Solid-state diffusion, or volume diffusion, is a mineral and trace element specific, temperature-dependent process that is typically slow in minerals, but can become significant at high temperatures found in the Earth's crust (Glicksman, 2000; Borg and Dienes, 2012). The presence of crystal defects, such as atomic vacancies and dislocations, will modify the diffusion characteristics of a mineral compared to a pristine crystal lattice. In the case of dislocations, faster diffusion may take place along the dislocation core (Love, 1964), with the result that bulk diffusion through the mineral will be faster or will be promoted at lower temperatures (Lee, 1995). During crystal-plastic deformation, dislocations and the impurities contained in their Cottrell atmospheres can migrate and

* Corresponding author. School of Earth and Planetary Sciences, The Institute for Geoscience Research (TIGeR), Curtin University, GPO Box U1987, Perth, WA, 6845, Australia.
E-mail address: denis.fougerouse@curtin.edu.au (D. Fougerouse).
Peer-review under responsibility of China University of Geosciences (Beijing).

https://doi.org/10.1016/j.gsf.2018.03.010

accumulate in low- and high-angle boundaries (Cottrell and Bilby, 1949). This migration process may take place at the same time as diffusion along the dislocation core and the relative importance of these two processes will be determined by the core diffusivity and the migration velocity of the dislocation (Cahn and Balluffi, 1979). Once formed, low- and high-angle boundaries may further promote fast diffusion (Joesten, 1991).

In polymetamorphic terrains, discriminating between the dominant mechanism for element mobility and the origin of elemental impurities, whether redistributed from within the grain (Reddy et al., 2006; Massey et al., 2011; Piazolo et al., 2016) or externally sourced (Klinger and Rabkin, 1998; Chen and Schuh, 2006) requires a robust temporal framework. Pb is a potentially useful trace element to establish such a framework as it comprises temporally-evolving radiogenic isotopic components, which can be used to discriminate Pb incorporated at the time of growth from Pb that was subsequently introduced. However, the characterisation of the Pb distribution and isotopic composition of specific microstructures and crystal defects has been difficult because the nanometre scale of these features are far smaller than the typical analytical volumes needed for measurement by most mass spectrometer techniques. Atom probe microscopy has successfully been used to provide new insights into the composition of such nanoscale domains in zircon (Valley et al., 2014; Peterman et al., 2016; Piazolo et al., 2016; Reddy et al., 2016), baddeleyite (White et al., 2017), monazite (Fougerouse et al., 2018) and titanite (Kirkland et al., 2018).

In this paper, electron backscatter diffraction (EBSD) and atom probe microscopy (APM) are combined to establish the relationship among deformation microstructures, trace element distributions and Pb isotopic composition in deformed pyrite from the Witwatersrand basin (South Africa). Pyrite is one of Earth's most abundant sulphide minerals and is often associated with ore deposits, particularly gold. The trace elements composition of pyrite has been used to decipher the origin, timing and condition of formation of ore deposits (Huston et al., 1995; Meffre et al., 2008; Large et al., 2009), as a vectoring tool for mineral exploration (Cassidy et al., 1998; Belousov et al., 2016) and as a proxy for paleoclimate studies (Large et al., 2014). This use of pyrite assumes that the composition of pyrite remains unchanged from the time of crystallisation and is unaffected by secondary process. Our study will challenge this assumption and will provide a framework for understanding the processes that may potentially modify trace element compositions of pyrite as well as other minerals.

2. Geological background

The studied sample is a quartz-dominated, poorly-sorted, clast-supported conglomerate from the Welkom region of the Witwatersrand Basin (South Africa; Fig. 1A). The Witwatersrand Basin unconformably lies on the 3.7–3.1 Ga basement of the Kaapvaal Craton (De Wit et al., 1992) and comprises a series of conglomerates that contain abundant quartz pebbles and detrital heavy minerals including rounded and framboidal detrital pyrites, uraninite and gold. The Witwatersrand conglomerates were deposited between 3096 Ma and 2714 Ma (Armstrong et al., 1991; Robb et al., 1991) and were subsequently overprinted by metamorphism, and associated hydrothermal activity, at greenschist facies ($T = 350 \pm 50$ °C; $P = 3$ kbar) (Phillips and Law, 1994; Frimmel and Gartz, 1997; Law and Phillips, 2005). The timing of this metamorphism spanned from 2.12 Ga in the Welkom goldfield to 2.06 Ga elsewhere in the basin (Gibson and Stevens, 1998; Alexandre et al., 2006; Rasmussen et al., 2007) and led to local Au remobilisation and formation of secondary sulphides including galena, pyrite and pyrrhotite (Frimmel et al., 1993; Robb and Meyer, 1995).

This study focuses on a well-characterized, deformed, round, compact pyrite grain from the Welkom Goldfield of the Witwatersrand Basin (Reddy and Hough, 2013). This detrital grain is overgrown by a narrow rim of fine-grained pyrrhotite (Fig. 1).

3. Methods

The analysed pyrite grain is one of the rounded, detrital varieties common in the conglomerates and has been previously examined

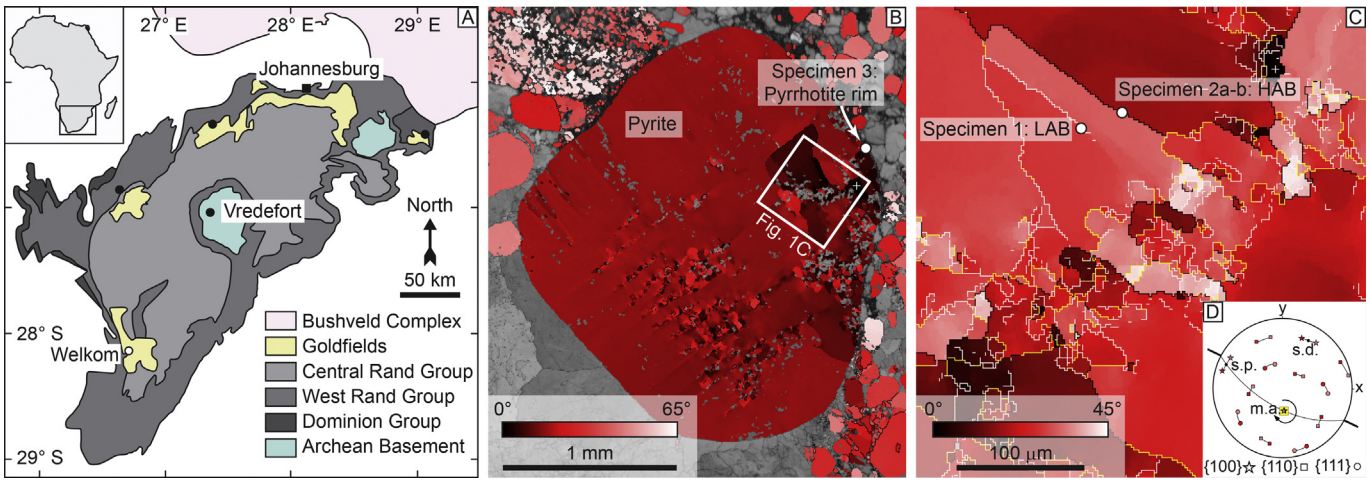

Figure 1. Geological map and EBSD data. (A) Simplified geological map of the Witwatersrand basin Modified after (Rasmussen et al., 2007); (B–D) EBSB data modified from Reddy and Hough (2013); (B) Crystallographic orientation electron backscattered diffraction (EBSD) map. Misorientation is colour coded from reference point "+" to maximum of 65°. High-angle boundaries (>10°) are plotted in black); (C) Detailed EBSD map colour coded to maximum of 45°. High-angle boundaries (HAB) (>10°) are plotted in black, low-angle boundaries (LAB) in white (>5° and <10°) and yellow (>2° and <5°). The location of atom probe specimen are indicated on B and C; (D) Lower hemisphere, equal area projection of pyrite lattice orientations at site of atom probe specimen 2. Data show orientations from 50 diffraction patterns. Crystallographic axes, shown by different symbols, are coloured to show the different lattice orientations following the colours in C. The dispersion across the boundary is illustrated by the single black line between symbols of different colours and is centred around a single (100) pole. Misorientation axes across the boundary ($n = 9$) fall within the yellow square and are parallel to the single (100) axis around which the crystal lattice is dispersed. The trace of the orientation boundary on the EBSD map (C) is shown by the thick black lines outside the primitive circle. A great circle connecting this trace and the misorientation/dispersion axes (m.a.) can be used to infer the orientation of the pole to slip plane (s.p.) and the slip direction (s.d.) associated with dislocation creep.

Please cite this article in press as: Fougerouse, D., et al., Time-resolved, defect-hosted, trace element mobility in deformed Witwatersrand pyrite, Geoscience Frontiers (2018), https://doi.org/10.1016/j.gsf.2018.03.010

by EBSD and electron microprobe (Reddy and Hough, 2013). A thin section of the conglomerate was prepared normal to bedding, and polished with progressively finer grades of diamond paste (9–1 μm) and final stage of 60 nm colloidal silica in a NaOH solution (pH 10). The sample was coated with a thin, ~5 nm film of carbon to inhibit specimen charging during scanning electron microscopy.

3.1. Electron backscatter diffraction

EBSD data were collected using a W-sourced Zeiss EVO scanning electron microscopes (SEMs), housed at Curtin University, Perth. SEM and electron backscatter patterns (EBSP) collection settings are reported in detail elsewhere (Reddy and Hough, 2013). Orientation maps were created by collecting and indexing an EBSD pattern from each node of a user-defined grid using Oxford Instruments' Channel 5 Flamenco software. Diffraction patterns were automatically indexed, for mean angular deviations <1°, to theoretical (hkl) reflector intensities of the different Kikuchi bands of pyrite using crystallographic data from Brostigen and Kjekshus (1969). EBSD data were noise reduced using standard "wildspike" and six-neighbour zero solution extrapolation approaches (Reddy and Hough, 2013). Post-processing of EBSD data was undertaken using Tango and Mambo components of the Channel 5 software.

3.2. Focused ion beam SEM

Site-specific, needle-shaped specimens for APM were prepared at Curtin University using a Tescan LYRA3 Ga^+ Focused Ion Beam-Scanning Electron Microscope (FIB-SEM). A 30 kV accelerating voltage ion beam at progressively lower beam currents was used to extract and sharpen the atom probe specimens with a final 2 kV accelerating voltage polishing step being performed to remove the beam damaged, Ga-implanted layer (Thompson et al., 2007; Fougerouse et al., 2016b).

3.3. Atom probe microscopy

APM was performed using a CAMECA LEAP 4000X HR at the Geoscience Atom Probe laboratory, part of the Advanced Resource Characterisation Facility and housed in the John de Laeter Centre, Curtin University. All specimens were analysed at a base temperature between 30 K and 50 K in laser-pulsing mode using an ultraviolet laser ($\lambda = 355$ nm) and pulse energy between 10 pJ and 50 pJ. The laser was pulsed at 125 kHz, with a detection rate of 1%. Ionic species were identified by time-of-flight mass spectrometry and graphed on a mass-to-charge spectrum (Fig. 2). Peaks which heights were twice above the background were identified and ranged using IVAS 3.6.14 for each datasets. Ranged ionic species were reconstructed in 3 dimensions using the impact event co-ordinates on the position sensitive detector and the succession of event. Details of analytical and reconstruction parameters are given in Supplementary Data Table 1 following recommendations of Blum et al. (2018). Subsets of the datasets were isolated using arbitrary isoconcentration surfaces (0.15 At.% Sb for specimen 1; 1.6 At.% As for specimen 2a and 2b; 0.08 At.% Pb for specimen 3) to extract the mass spectra of specific domains (Hellman et al., 2000). This approach allows the background noise to be significantly reduced and improves detection limits of trace elements.

Pb isotopic compositions were quantified following the approaches outlined in previous studies of zircon (Peterman et al., 2016). A fixed width (0.41 Da) was used for ranging each isotope peak (Fig. 2 inset) and isotopic abundances were quantified by subtracting the estimated background counts from each identified Pb peak. The local background signal was measured from the counts in a wide 'peak-free' range (3 Da) in close proximity to the Pb^{++} peaks. These background counts were subsequently normalised to the width of the Pb peaks. Uncertainties for each background-corrected isotopic species were estimated from counting statistics for each isotope peak and its correction. The isotopic ratios uncertainties were consequently derived from the uncertainty of each species used for calculating the ratio and reported at 1σ (Tables 1 and S2).

4. Results

EBSD analysis indicates that the pyrite comprises domains recording complex, but systematic, microstructural relationships. These were previously shown to reflect crystal plasticity associated with dislocation creep (Reddy and Hough, 2013). Within this microstructural framework 4 specimens were selected for APM

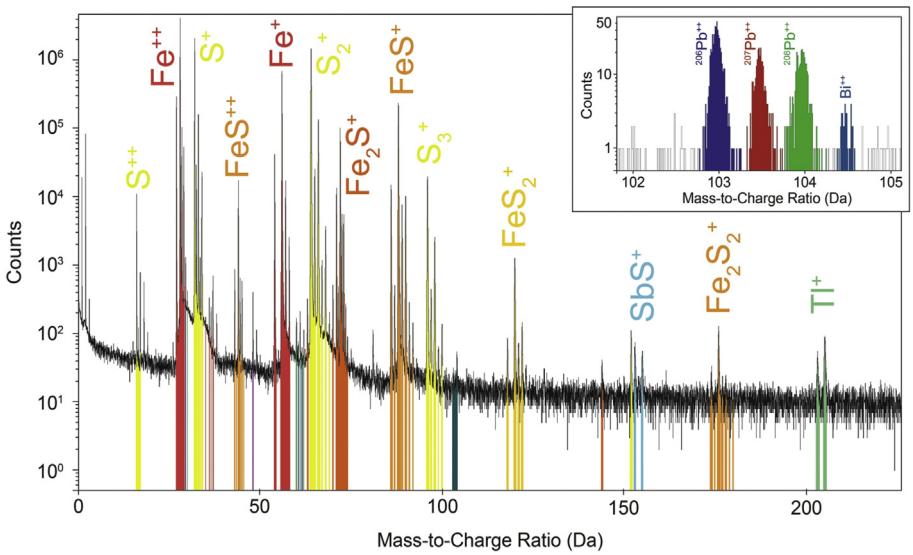

Figure 2. Atom probe mass spectrum of pyrite. Representative atom probe microscopy mass spectrum. Peaks are colour-coded by molecular species and/or element. Inset: Mass spectrum for atoms local to the high-angle boundary (specimen 2a) showing distinct mass peaks for ^{206}Pb, ^{207}Pb and ^{208}Pb.

Please cite this article in press as: Fougerouse, D., et al., Time-resolved, defect-hosted, trace element mobility in deformed Witwatersrand pyrite, Geoscience Frontiers (2018), https://doi.org/10.1016/j.gsf.2018.03.010

Table 1
Composition of microstructural domains. Major and trace element composition in At.%. Pb* correspond to background-corrected counts. The uncertainty is estimated from counting statistics for each isotope peak and its background correction. Background-corrected $^{207}Pb/^{206}Pb$ ratios are reported with 1σ uncertainty. Pb isotopic composition are given for Pb-enriched domains only.

Specimen	1 - LAB		2a -HAB		2b - HAB		3 - Rim	
Domain	Whole	ROI	Whole	ROI	Whole	ROI	Whole	ROI
Fe	38.7	36.1	40.5	36.7	37.6	34.1	52.3	52.4
S	61.2	61.0	57.8	56.4	62.1	60.3	47.6	47.1
As	-	-	0.744	3.433	0.123	2.950	-	-
Ni	0.010	1.115	0.541	1.928	0.085	1.420	-	-
Co	0.008	0.049	0.329	1.234	0.059	0.930	0.027	0.079
Sb	0.003	0.463	0.013	0.063	0.003	0.059	-	-
Pb	0.001	0.213	0.026	0.116	0.006	0.087	-	0.267
Bi	-	-	0.009	0.044	0.002	0.038	-	-
Ge	0.008	0.028	0.021	0.020	0.006	0.008	0.008	0.022
Tl	0.005	0.989	-	-	-	-	-	-
$^{206}Pb^*$	-	58 ± 8	-	545 ± 24	-	209 ± 14	-	51 ± 7
$^{207}Pb^*$	-	68 ± 8	-	256 ± 16	-	89 ± 10	-	12 ± 3
$^{208}Pb^*$	-	164 ± 13	-	290 ± 17	-	101 ± 10	-	6 ± 2
$^{207}Pb^*/^{208}Pb^* \pm 1\sigma$	-	0.41 ± 0.06	-	0.88 ± 0.08	-	0.88 ± 0.13	-	2.00 ± 1.00
$^{206}Pb^*/^{208}Pb^* \pm 1\sigma$	-	0.35 ± 0.06	-	1.88 ± 0.14	-	2.07 ± 0.25	-	8.50 ± 3.67

analysis of three distinct microstructural domains (Fig. 1B and C). The first specimen is located within 1 μm of a 1°–2° low-angle boundary. Specimens 2a and 2b targeted a high-angle (15°) boundary. In detail, the trace of this boundary on the orientation map (Fig. 1C) and the misorientation characteristics across the boundary (Fig. 1D) show the boundary is a {100} plane of the pyrite and is geometrically-consistent with the formation and migration of dislocations associated with a {100}<010> slip system (Fig. 1D). The fine-grained pyrrhotite rim overgrowing the pyrite crystal constitutes specimen 3 and represents the last stage of sulphide crystallization in the sample.

Atom probe data for pyrite and pyrrhotite are reported in mass-to-charge ratio spectra and include a complex suite of single element and molecular species (Figs. 2 and S-1). Three Pb peaks are present in the mass spectrum as Pb^{++} at 103, 103.5 and 104 Da (Fig. 2) representing $^{206}Pb^{++}$, $^{207}Pb^{++}$ and $^{208}Pb^{++}$, respectively. No peak associated with ^{204}Pb was identified above the background noise and no U or Th were detected in any of the datasets.

Reconstruction of the atom probe data of specimen 1 shows the presence of two curvilinear features highlighted by an enrichment in Sb, Ni and a slight increase in Pb and Tl (Fig. 3 and Table 1). A ~20 nm spheroidal cluster enriched in Pb, Sb, Ni, Cu and Tl is

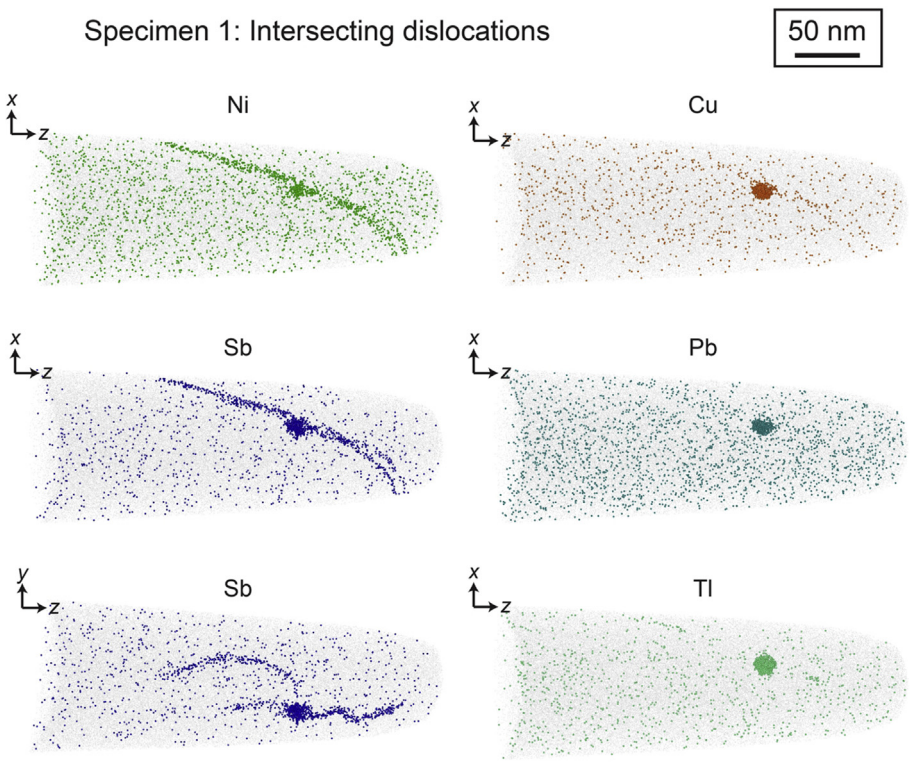

Figure 3. Atom probe 3D reconstruction of specimen 1. Pb, Sb, Ni, Cu and Tl cluster at the intersection of two dislocations highlighted by Sb and Ni.

Please cite this article in press as: Fougerouse, D., et al., Time-resolved, defect-hosted, trace element mobility in deformed Witwatersrand pyrite, Geoscience Frontiers (2018), https://doi.org/10.1016/j.gsf.2018.03.010

located at the intersection of the linear features. The Pb isotopic ratios for the cluster are 0.41 ± 0.06 for $^{207}Pb/^{208}Pb$ and 0.35 ± 0.06 for $^{206}Pb/^{208}Pb$, whereas no Pb peaks in the rest of the specimen could be measured above the background noise.

The high-angle boundary (15° misorientation) in specimen 2a is marked by a planar feature with a core and shell structure. The 5 nm wide core is decorated by Pb, Sb and Bi (Fig. 4 and Table 1). The wider (10 nm) shell has a significant enrichment in As, Ni and Co, with up to 8 At. % increase in those elements compared to the bulk of the pyrite (Table 1). The distribution of the enriched elements along the boundary is heterogeneous, as demonstrated by small, poorly defined clusters with diameters of 5–10 nm (Fig. 4).

The Pb composition of the analysed portion of the high-angle boundary is 0.88 ± 0.08 for the $^{207}Pb/^{208}Pb$ ratio and 1.88 ± 0.14 for the $^{206}Pb/^{208}Pb$ ratio. Similar trace element distributions and Pb composition were observed for specimen 2b (Fig. S-2) with Pb isotopic ratios of 0.88 ± 0.13 and 2.07 ± 0.25 for $^{207}Pb/^{208}Pb$ and $^{206}Pb/^{208}Pb$, respectively. No statistically significant Pb isotopic variations could be discriminated within the high-angle boundary of specimen 2a and 2b.

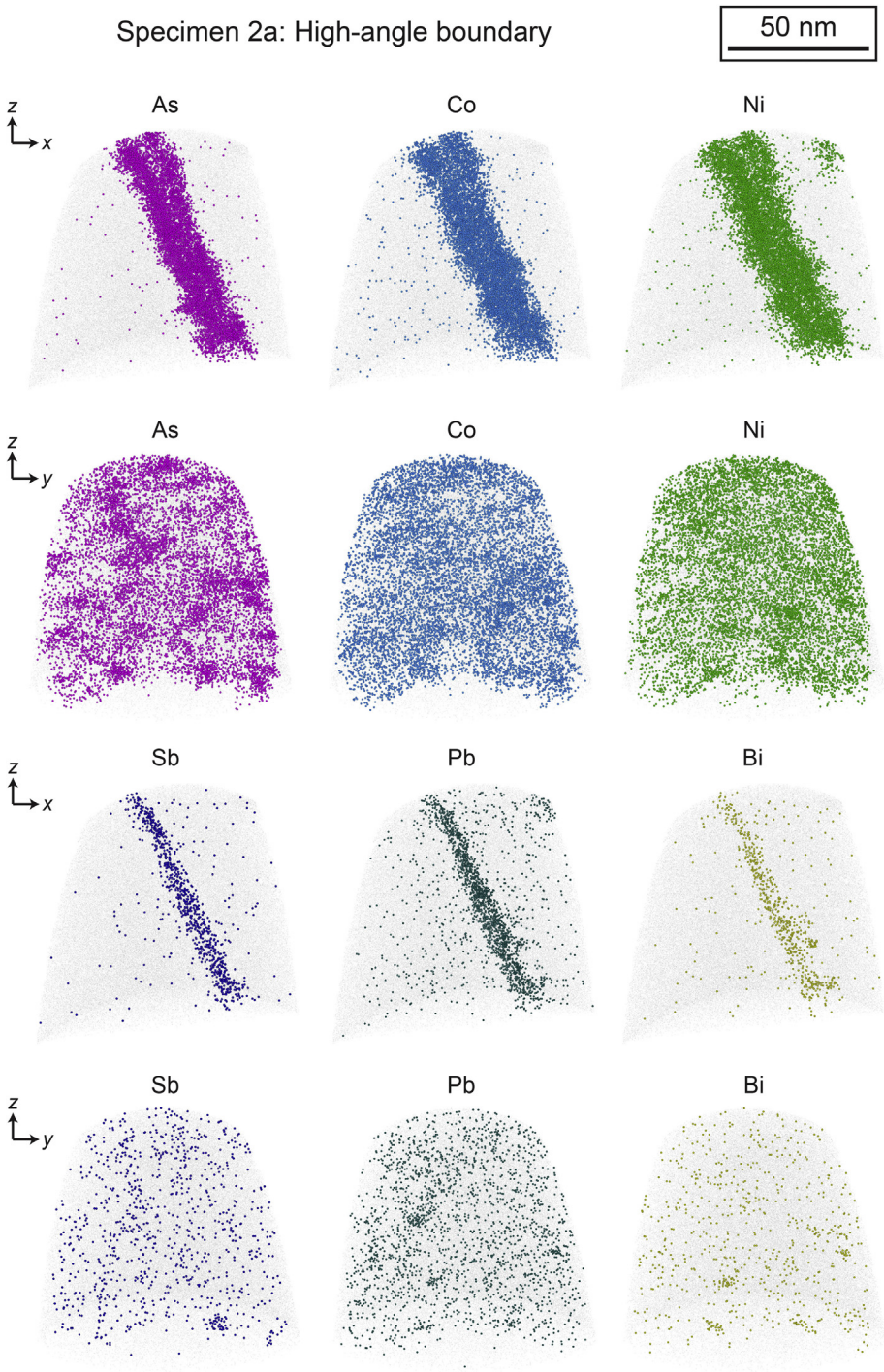

Figure 4. Atom probe 3D reconstruction of specimen 2a. As, Co, Ni, Sb, Pb and Bi are enriched in the high-angle boundary (12° misorientation). The lateral distribution of elements along the boundary is heterogeneous with clusters.

Please cite this article in press as: Fougerouse, D., et al., Time-resolved, defect-hosted, trace element mobility in deformed Witwatersrand pyrite, Geoscience Frontiers (2018), https://doi.org/10.1016/j.gsf.2018.03.010

In the pyrrhotite rim (specimen 3; Fig. 5), the nanoscale distribution of Pb is marked by a single linear feature enriched solely in Pb (Table 1). No Pb peaks could be identified above the background for the domain surrounding the dislocation. The Pb isotopic ratios of this feature are 2.00 ± 1.00 for $^{207}Pb/^{208}Pb$ and 8.50 ± 3.67 for $^{206}Pb/^{208}Pb$.

5. Discussion

5.1. Pyrite microstructures and relationship to trace element distribution

Internally, the pyrite grain records a complex deformation-related microstructure associated with the formation of high (>10°) and low-angle (<10°) grain boundaries (Fig. 1B and C). Reddy and Hough (2013) previously established that this deformation microstructures took place prior to the erosion, transportation and redeposition of the detrital pyrite within the Welkom conglomerate, and therefore shortly after initial crystallisation. The microstructures of the pyrite grain, including the high-angle boundary analysed in specimen 2a and 2b, are consistent with sub-grain rotation recrystallization with the activity of the <100> {010} slip system and the mobility of the common pyrite dislocations (Reddy and Hough, 2013). In the host pyrite, at least two symmetrically-equivalent dislocation geometries operate at 90° to each other (Reddy and Hough, 2013). Such geometrical relationships between dislocations are consistent with the linear features observed in specimen 1, which we interpret to be dislocations.

In specimen 1, Pb, Sb, Ni, Cu and Tl decorate the dislocations, but are also concentrated in a small, 20 nm spheroidal cluster at the intersection of two dislocations. As, Ni, Co, Pb, Sb and Bi enriched in a high-angle boundary (specimens 2a and 2b) that displays clustering of the trace elements along the plane of the boundary and, Pb in pyrrhotite is located in a single linear feature. Because the pyrrhotite postdates all deformation in the sample and is microscopically undeformed, this dislocation interpreted to represent a growth-related defect (Klapper, 2010). The nanoscale distribution of trace elements is therefore complex. Nonetheless, there is a clear spatial relationship between trace element enrichment and the presence of microstructures.

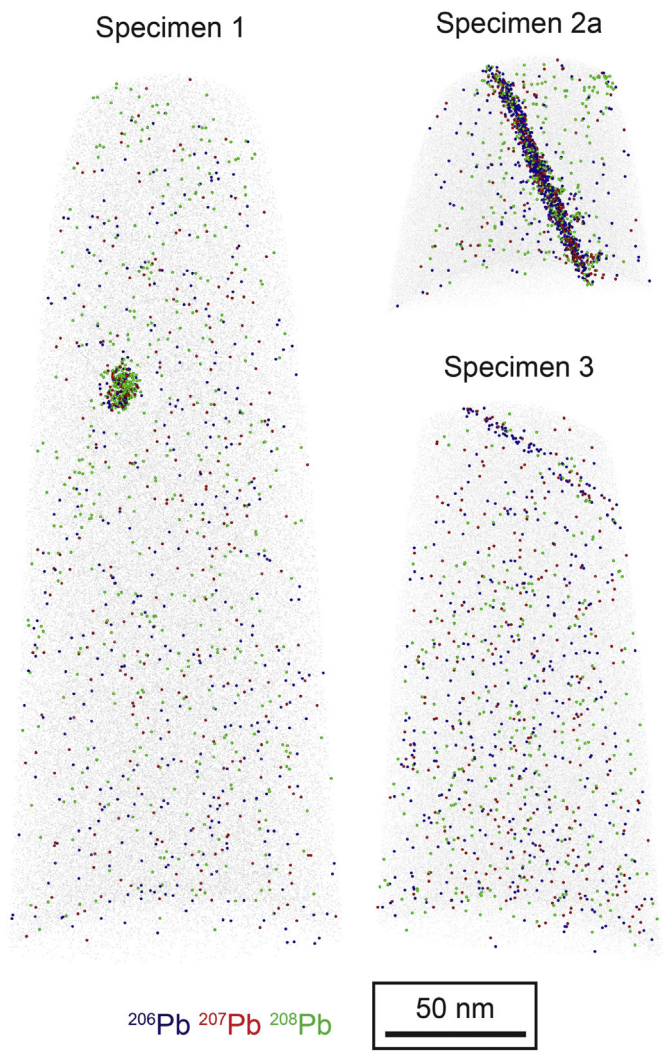

Figure 5. Atom probe 3D reconstructions. Each sphere represents a Pb atom; Dark green: all Pb atoms; Blue: ^{206}Pb; Red: ^{207}Pb; Light green: ^{208}Pb. A single dislocation is highlighted by Pb in specimen 3.

5.2. Pb isotopic compositions and sources

The pyrite grain contains no detectable U or Th and, therefore, all measured Pb is a component either inherited during growth or subsequently added to the grain. The atom probe data indicate that the Pb isotopic composition of the studied pyrite grain is heterogeneous. The isotopic composition of Pb provides constraints on possible sources, and can be used visualise the 3-D distribution of different common Pb components and how these relate to the different microstructures (Figs. 5 and 6).

The composition of the Pb cluster defined by the intersecting dislocations (specimen 1) is consistent with a terrestrial common Pb model composition at 3.0 Ga (Stacey and Kramers, 1975). This interpretation is compatible with previous analyses of the 'least radiogenic' pyrites intercepting the common Pb evolution curve at ~3.0 Ga and defines the Pb isotopic signature at the time of initial crystallisation of the pyrite (Koppel and Saager, 1974; Barton and Hallbauer, 1996; Large et al., 2013).

The Pb composition of the pyrrhotite overgrowing rim is characterised by an inherited radiogenic Pb composition and plots

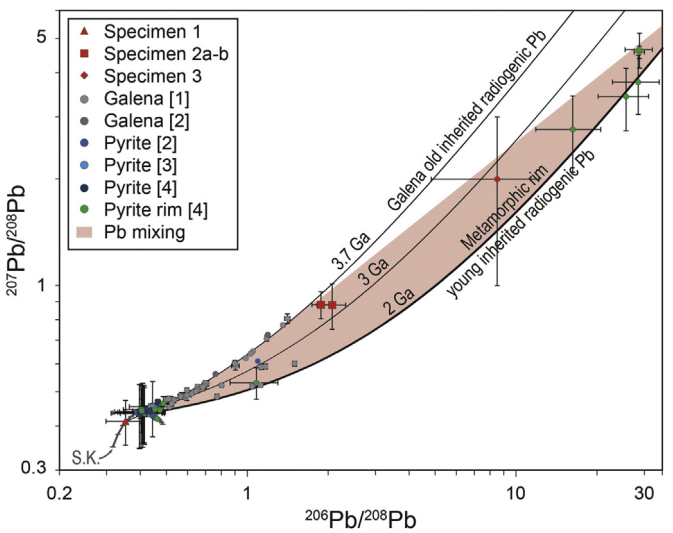

Figure 6. Pb isotopic data. Pb isotope data from this and previous studies, [1] Burger et al., 1962; [2] Koppel and Saager, 1974; [3] Barton and Hallbauer, 1996; [4] Large et al., 2013. The field coloured in pink represent the mixing of three distinct Pb reservoirs with a ~3.0 Ga common Pb reservoir (epigenetic, vein-hosted gold deposit), an old inherited radiogenic 3.7 Ga Pb (Kaapvaal craton) and a young inherited radiogenic ~2.0 Ga Pb (breakdown of uraninite during regional metamorphism).

Please cite this article in press as: Fougerouse, D., et al., Time-resolved, defect-hosted, trace element mobility in deformed Witwatersrand pyrite, Geoscience Frontiers (2018), https://doi.org/10.1016/j.gsf.2018.03.010

between 3.0 Ga and 2.0 Ga isochron (Fig. 6). The low number of atoms imaged by atom probe result in large uncertainties for this domain, highlighting that care should be given in interpreting these data. However, previous Laser Ablation – Inductively Coupled Plasma Mass Spectrometry (LA-ICPMS) analyses of pyrite metamorphic rims from other samples define a ~2.0 Ga isochron and indicate mixing between a non-radiogenic common Pb source and a 2.0 Ga inherited radiogenic Pb source, consistent with our atom probe data (Large et al., 2013). The 2.0 Ga age of the metamorphic rims corresponds to the regional greenschist metamorphism and the breakdown of uraninite (Burger et al., 1962; Depiné et al., 2013), determined by U–Pb in monazite and xenotime (Kositcin et al., 2003; Rasmussen et al., 2007). Uraninite is abundant in the Witwatersrand conglomerates and is a probable source for the unsupported, common radiogenic Pb component analysed in the pyrrhotite rim.

The isotopic composition of Pb in the high-angle boundary is not consistent with a 3.0 Ga radiogenic Pb composition (Fig. 6). Instead, previously reported galena analyses define an apparent 3.7 Ga isochron (Burger et al., 1962; Koppel and Saager, 1974). This isochron intercepts the common Pb evolution curve at ~3.0 Ga and is interpreted to indicate mixing between 3.0 Ga common Pb and an old (3.7 Ga) inherited radiogenic Pb component. The origin of this 3.7 Ga Pb is unconstrained, nonetheless, a 3.7 Ga age is coeval with the early stages of Kaapvaal basement formation and production from crustal U may represent the source of this Pb (De Wit et al., 1992). However, the Pb composition of the high-angle boundary deviates from the 3.7 Ga and 3.0 Ga isochrons indicating mixing with young Pb, either the 3.0 Ga common Pb from pyrite crystallisation or the 2.0 Ga inherited radiogenic Pb.

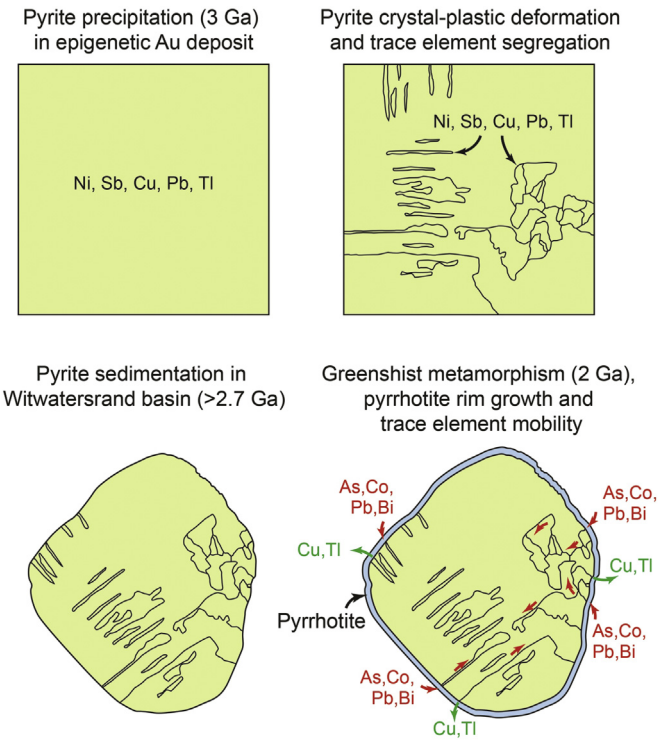

Figure 7. Interpretative diagram. Interpretation of the trace element mobility during deformation and metamorphism. The trace element budget is redistributed during deformation and subsequently overprinted during metamorphism.

5.3. Mechanisms and timing of trace element mobility

The site-specific targeting of microstructural features by APM places valuable constraints on trace element mobility in pyrite. The cluster of Pb, Sb, Ni, Cu and Tl identified in specimen 1 forms at the intersection of two oblique dislocations, each marked by an enrichment in Sb, Ni and Pb (Fig. 3). The presence of Sb and Ni enrichment along the intersecting dislocations is not consistent with the dislocations having been pinned by a pre-existing cluster. A more likely scenario is the migration and entanglement of the dislocations in a Forest-type interaction (Zhou et al., 1998; Wickham et al., 1999) creating a core-core overlap region favourable for hosting large ionic radii impurities (Zhou et al., 1998).

The data of specimen 1 indicate that Pb, Sb, Ni, Cu and Tl was able to migrate within the dislocations and this may have taken place by migration along the dislocation core (Johnston and Gilman, 1959) or in the distorted crystal lattice surrounding the dislocation (Cottrell and Bilby, 1949). There is a large size discrepancy between the ionic radii of Pb^{2+}, Tl^{+} and Fe^{2+}, irrespective of coordination number (Shannon, 1976). This could inhibit lattice diffusion at the low temperature metamorphic conditions experienced by the Witwatersrand pyrite, and precludes the mobility of Pb and Tl by a Cottrell atmosphere process. However, the slightly smaller size of Ni^{2+} compared to Fe^{2+}, can explain the presence of Ni in the dislocations and may be interpreted to be trapped in Cottrell atmospheres (Cottrell and Bilby, 1949; Shannon, 1976). The observation of ionic species with widely different atomic radii suggests that both mechanisms may have been active in pyrite.

The atom probe data of specimen 1 are consistent with a dynamic process of mobile dislocations collecting Pb, Sb, Ni, Cu and Tl as they migrated through the pyrite lattice (Fig. 7), accompanied by fast diffusion of the captured trace elements along the dislocation core (Love, 1964). Significantly, the diffusion of Pb along dislocations did not lead to the complete loss of Pb from the mineral, or exchange with a younger Pb reservoir. Instead, Pb became fixed in the core-core overlap region of dislocation intersections. Since minerals deforming by crystal plastic dislocation processes necessitate the operation of 5 slip systems (von Mises condition; Groves and Kelly, 1963), then dislocation intersections in pyrite are expected to be common. The ability of dislocations to facilitate grain-scale Pb mobility in pyrite will therefore be limited by the entrapment of Pb at dislocation intersections. This has potential importance for other Pb-bearing minerals such as zircon, where dislocations in deformed grains have been suggested as a possible pathway for the resetting of Pb isotope compositions (Moser et al., 2009; Nemchin et al., 2009; Piazolo et al., 2016).

The trace element composition of the high-angle boundary (specimen 2a and 2b) is different compared to the cluster observed in specimen 1 with the presence of As, Co, Bi and the absence of Cu and Tl. The core (Pb, Sb, Bi) and shell (As, Co, Ni) structure of the boundary may be explained by a ionic radii organisation with the larger ions located in the centre of the boundary. The Pb isotopic composition of the core of the high-angle boundary however indicates a three component mixing between ~3.0 Ga common Pb, old 3.7 Ga inherited radiogenic Pb and young ~2.0 Ga inherited radiogenic Pb. The interaction between the three distinct Pb reservoirs indicates that the high-angle boundary behaved as an open system during the 2.0 Ga metamorphism. This open system behaviour also explains the addition of As, Co and Bi, which are absent from specimen 1, to the boundary and the simultaneously loss of Cu and Tl. The data suggest that the high-angle boundary formed part of a network (Fig. 1), which acted as a 10 nm wide, fast diffusion pathway and permitted chemical exchange with the crystal surface (Fig. 7). The open system behaviour took place approximately 1 billion years after the formation of the deformation microstructures, and was contemporaneous with low-grade metamorphism. This data highlights the critical role

Please cite this article in press as: Fougerouse, D., et al., Time-resolved, defect-hosted, trace element mobility in deformed Witwatersrand pyrite, Geoscience Frontiers (2018), https://doi.org/10.1016/j.gsf.2018.03.010

deformation–related defects and microstructures may play in controlling element mobility over long periods of geological time.

The study reveals mixing of three different Pb sources in the Witwatersrand sulphides with the interaction of a ~3.0 Ga common Pb reservoir (epigenetic, vein-hosted gold deposit), an old inherited radiogenic 3.7 Ga Pb (Kaapvaal craton) and a young inherited radiogenic ~2.0 Ga Pb (breakdown of uraninite during regional metamorphism) along the deformation microstructures network.

The processes identified in this study operate at the nanoscale and can be uniquely resolved by atom probe analysis of distinct microstructural sites. Our results, provide new insights into the mechanisms responsible for Pb and trace element mobility in pyrite that may also operate in other accessory phases commonly used for Pb isotopic dating. Hence, the nanoscale, time-integrated, 3-D mapping of trace elements has significant potential for constraining the processes responsible for the compositional modification of minerals.

Acknowledgments

The authors would like to acknowledge constructive reviews by Lee White, Phillip Gopon and editorial handling by Andrew Putnis. The Australian Resource Characterisation Facility (ARCF), under the auspices of the National Resource Sciences Precinct (NRSP) – the collaboration between CSIRO, Curtin University and The University of Western Australia – is supported by the Science and Industry Endowment Fund (SIEF RI13-01). The authors gratefully acknowledge support of Curtin University's Microscopy & Microanalysis Facility and the John de Laeter Centre, whose instrumentation has been supported by University, State and Commonwealth Government funding. SMR acknowledges support from the ARC Core to Crust Fluid System COE (CE11E0070) and the SIEF Distal Footprints program (RP04-063).

Appendix A. Supplementary data

Supplementary data related to this article can be found at https://doi.org/10.1016/j.gsf.2018.03.010.

References

Alexandre, P., Andreoli, M.A., Jamison, A., Gibson, R.L., 2006. 40 Ar/39 Ar age constraints on low-grade metamorphism and cleavage development in the Transvaal Supergroup (central Kaapvaal craton, South Africa): implications for the tectonic setting of the Bushveld Igneous Complex. South African Journal of Geology 109 (3), 393–410.

Ando, J., Shibata, Y., Okajima, Y., Kanagawa, K., Furusho, M., Tomioka, N., 2001. Striped iron zoning of olivine induced by dislocation creep in deformed peridotites. Nature 414 (6866), 893–895.

Armstrong, R., Compston, W., Retief, E., Williams, I.t., Welke, H., 1991. Zircon ion microprobe studies bearing on the age and evolution of the Witwatersrand triad. Precambrian Research 53 (3–4), 243–266.

Barton, E., Hallbauer, D., 1996. Trace-element and U- Pb isotope compositions of pyrite types in the proterozoic black reef, transvaal sequence, South Africa: implications on genesis and age. Chemical Geology 133 (1), 173–199.

Belousov, I., Large, R., Meffre, S., Danyushevsky, L., Steadman, J., Beardsmore, T., 2016. Pyrite compositions from VHMS and orogenic Au deposits in the Yilgarn Craton, Western Australia: implications for gold and copper exploration. Ore Geology Reviews 79, 474–499.

Blum, T.B., Darling, J.R., Kelly, T.F., Larson, D.J., Moser, D.E., Perez-Huerta, A., Prosa, T.J., Reddy, S.M., Reinhard, D.A., Saxey, D.W., 2018. Best practices for reporting atom probe analysis of geological materials. Microstructural Geochronology: Planetary Records Down to Atom Scale 369–373.

Borg, R.J., Dienes, G.J., 2012. An Introduction to Solid State Diffusion. Elsevier.

Brostigen, G., Kjekshus, A., 1969. Redetermined crystal structure of FeS2 (pyrite). Acta Chem Scand 23, 2186–2188.

Burger, A., Nicolaysen, L., De Villiers, J., 1962. Lead isotopic compositions of galenas from the Witwatersrand and orange free state, and their relation to the Witwatersrand and dominion reef uraninites. Geochimica et Cosmochimica Acta 26 (1), 25IN551–50IN659.

Büttner, S.H., Kasemann, S.A., 2007. Deformation-controlled cation diffusion in tourmaline: a microanalytical study on trace elements and boron isotopes. American Mineralogist 92 (11–12), 1862–1874.

Cahn, J., Balluffi, R., 1979. Diffusional Mass Transport in Polycrystals Containing Stationary or Migrating Grain Boundaries. Massachusetts Inst. of Tech., Cambridge (USA).

Cassidy, K.F., Groves, D.I., McNaughton, N.J., 1998. Late-Archean granitoid-hosted lode-gold deposits, Yilgarn Craton, Western Australia: deposit characteristics, crustal architecture and implications for ore genesis. Ore Geology Reviews 13 (1), 65–102.

Chen, Y., Schuh, C.A., 2006. Diffusion on grain boundary networks: percolation theory and effective medium approximations. Acta Materialia 54 (18), 4709–4720.

Cottrell, A.H., Bilby, B., 1949. Dislocation theory of yielding and strain ageing of iron. Proceedings of the Physical Society Section A 62 (1), 49.

De Wit, M.J., de Ronde, C.E., Tredoux, M., Roering, C., Hart, R.J., Armstrong, R.A., Green, R.W., Peberdy, E., Hart, R.A., 1992. formation of an archaean continent. Nature 357 (6379), 553–562.

Depiné, M., Frimmel, H., Emsbo, P., Koenig, A., Kern, M., 2013. Trace element distribution in uraninite from Mesoarchaean Witwatersrand conglomerates (South Africa) supports placer model and magmatogenic source. Mineralium Deposita 48 (4), 423–435.

Fougerouse, D., Micklethwaite, S., Halfpenny, A., Reddy, S.M., Cliff, J.B., Martin, L.A., Kilburn, M., Guagliardo, P., Ulrich, S., 2016a. The golden ark: arsenopyrite crystal plasticity and the retention of gold through high strain and metamorphism. Terra Nova 28 (3), 181–187.

Fougerouse, D., Reddy, S.M., Saxey, D.W., Erickson, T.M., Kirkland, C.L., Rickard, W.D.A., Seydoux-Guillaume, A.M., Clark, C., Buick, I.S., 2018. Nanoscale distribution of Pb in monazite revealed by atom probe microscopy. Chemical Geology 479, 251–258.

Fougerouse, D., Reddy, S.M., Saxey, D.W., Rickard, W.D., Van Riessen, A., Micklethwaite, S., 2016b. Nanoscale gold clusters in arsenopyrite controlled by growth rate not concentration: evidence from atom probe microscopy. American Mineralogist 101 (8), 1916–1919.

Frimmel, H., Gartz, V., 1997. Witwatersrand gold particle chemistry matches model of metamorphosed, hydrothermally altered placer deposits. Mineralium Deposita 32 (6), 523–530.

Frimmel, H., Le Roex, A., Knight, J., Minter, W., 1993. A case study of the post-depositional alteration of the Witwatersrand Basal Reef gold placer. Economic Geology 88 (2), 249–265.

Gibson, R.L., Stevens, G., 1998. Regional metamorphism due to anorogenic intracratonic magmatism. Geological Society London Special Publications 138 (1), 121–135.

Glicksman, M.E., 2000. Diffusion in Solids: Field Theory, Solid-state Principles and Applications. Wiley.

Groves, G., Kelly, A., 1963. Independent slip systems in crystals. Philosophical Magazine 8 (89), 877–887.

Hellman, O.C., Vandenbroucke, J.A., Rüsing, J., Isheim, D., Seidman, D.N., 2000. Analysis of three-dimensional atom-probe data by the proximity histogram. Microscopy and Microanalysis 6 (05), 437–444.

Huston, D.L., Sie, S.H., Suter, G.F., Cooke, D.R., Both, R.A., 1995. Trace elements in sulfide minerals from eastern Australian volcanic-hosted massive sulfide deposits; Part I, Proton microprobe analyses of pyrite, chalcopyrite, and sphalerite, and Part II, Selenium levels in pyrite; comparison with delta 34 S values and implications for the source of sulfur in volcanogenic hydrothermal systems. Economic Geology 90 (5), 1167–1196.

Joesten, R., 1991. Grain-boundary Diffusion Kinetics in Silicate and Oxide Minerals. Diffusion, Atomic Ordering, and Mass Transport. Springer, pp. 345–395.

Johnston, W., Gilman, J.J., 1959. Dislocation velocities, dislocation densities, and plastic flow in lithium fluoride crystals. Journal of Applied Physics 30 (2), 129–144.

Kirkland, C.L., Fougerouse, D., Reddy, S.M., Hollis, J., Saxey, D., 2018. Assessing the mechanisms of common Pb incorporation into titanite. Chemical Geology. https://doi.org/10.1016/j.chemgeo.2018.03.026.

Klapper, H., 2010. Generation and Propagation of Defects during Crystal Growth. Springer Handbook of Crystal Growth. Springer, pp. 93–132.

Klinger, L., Rabkin, E., 1998. Diffusion along the grain boundaries in crystals with dislocations. Interface Science 6 (3), 197–203.

Koppel, V.H., Saager, R., 1974. Lead isotope evidence on the detrital origin of Witwatersrand pyrites and its bearing on the provenance of the Witwatersrand gold. Economic Geology 69 (3), 318–331.

Kositcin, N., McNaughton, N.J., Griffin, B.J., Fletcher, I.R., Groves, D.I., Rasmussen, B., 2003. Textural and geochemical discrimination between xenotime of different origin in the Archaean Witwatersrand Basin, South Africa. Geochimica et Cosmochimica Acta 67 (4), 709–731.

Large, R.R., Danyushevsky, L., Hollit, C., Maslennikov, V., Meffre, S., Gilbert, S., Bull, S., Scott, R., Emsbo, P., Thomas, H., 2009. Gold and trace element zonation in pyrite using a laser imaging technique: implications for the timing of gold in orogenic and Carlin-style sediment-hosted deposits. Economic Geology 104 (5), 635–668.

Large, R.R., Halpin, J.A., Danyushevsky, L.V., Maslennikov, V.V., Bull, S.W., Long, J.A., Gregory, D.D., Lounejeva, E., Lyons, T.W., Sack, P.J., McGoldrick, P.J., Calver, C.R., 2014. Trace element content of sedimentary pyrite as a new proxy for deep-time ocean–atmosphere evolution. Earth and Planetary Science Letters 389 (Suppl. C), 209–220.

Large, R.R., Meffre, S., Burnett, R., Guy, B., Bull, S., Gilbert, S., Goemann, K., Danyushevsky, L., 2013. Evidence for an intrabasinal source and multiple

concentration processes in the formation of the Carbon Leader Reef, Witwatersrand Supergroup, South Africa. Economic Geology 108 (6), 1215–1241.
Law, J., Phillips, G., 2005. Hydrothermal Replacement Model for Witwatersrand Gold. Economic Geology 100th Anniversary Volume, pp. 799–811.
Lee, J.K., 1995. Multipath diffusion in geochronology. Contributions to Mineralogy and Petrology 120 (1), 60–82.
Love, G., 1964. Dislocation pipe diffusion. Acta Metallurgica 12 (6), 731–737.
Massey, M.A., Prior, D.J., Moecher, D.P., 2011. Microstructure and crystallographic preferred orientation of polycrystalline microgarnet aggregates developed during progressive creep, recovery, and grain boundary sliding. Journal of Structural Geology 33 (4), 713–730.
McCaig, A., Covey-Crump, S.J., Ismaïl, W.B., Lloyd, G.E., 2007. Fast diffusion along mobile grain boundaries in calcite. Contributions to Mineralogy and Petrology 153 (2), 159–175.
Meffre, S., Large, R.R., Scott, R., Woodhead, J., Chang, Z., Gilbert, S.E., Danyushevsky, L.V., Maslennikov, V., Hergt, J.M., 2008. Age and pyrite Pb-isotopic composition of the giant Sukhoi Log sediment-hosted gold deposit, Russia. Geochimica et Cosmochimica Acta 72 (9), 2377–2391.
Moser, D., Davis, W., Reddy, S., Flemming, R., Hart, R., 2009. Zircon U–Pb strain chronometry reveals deep impact-triggered flow. Earth and Planetary Science Letters 277 (1), 73–79.
Nakagawa, T., Nakamura, A., Sakaguchi, I., Shibata, N., Mizoguchi, T., Yamamoto, T., Haneda, H., Ohashi, N., Ikuhara, Y., 2011. Cation diffusion along basal dislocations in sapphire. Acta Materialia 59 (3), 1105–1111.
Nemchin, A., Timms, N.E., Pidgeon, R., Geisler, T., Reddy, S., Meyer, C., 2009. Timing of crystallization of the lunar magma ocean constrained by the oldest zircon. Nature Geoscience 2, 133–136.
Peterman, E.M., Reddy, S.M., Saxey, D.W., Snoeyenbos, D.R., Rickard, W.D., Fougerouse, D., Kylander-Clark, A.R., 2016. Nanogeochronology of discordant zircon measured by atom probe microscopy of Pb-enriched dislocation loops. Science Advances 2 (9), e1601318.
Phillips, N.G., Law, J.D., 1994. Metamorphism of the Witwatersrand gold fields: a review. Ore Geology Reviews 9 (1), 1–31.
Piazolo, S., La Fontaine, A., Trimby, P., Harley, S., Yang, L., Armstrong, R., Cairney, J.M., 2016. Deformation-induced trace element redistribution in zircon revealed using atom probe tomography. Nature Communications 7.
Rasmussen, B., Fletcher, I.R., Muhling, J.R., Mueller, A.G., Hall, G.C., 2007. Bushveld-aged fluid flow, peak metamorphism, and gold mobilization in the Witwatersrand basin, South Africa: constraints from in situ SHRIMP U-Pb dating of monazite and xenotime. Geology 35 (10), 931–934.
Reddy, S.M., Hough, R.M., 2013. Microstructural evolution and trace element mobility in Witwatersrand pyrite. Contributions to Mineralogy and Petrology 166 (5), 1269–1284.
Reddy, S.M., Timms, N.E., Trimby, P., Kinny, P.D., Buchan, C., Blake, K., 2006. Crystal-plastic deformation of zircon: a defect in the assumption of chemical robustness. Geology 34 (4), 257–260.
Reddy, S.M., van Riessen, A., Saxey, D.W., Johnson, T.E., Rickard, W.D., Fougerouse, D., Fischer, S., Prosa, T.J., Rice, K.P., Reinhard, D.A., 2016. Mechanisms of deformation-induced trace element migration in zircon resolved by atom probe and correlative microscopy. Geochimica et Cosmochimica Acta 195, 158–170.
Robb, L.J., Davis, D., Kamo, S., 1991. Chronological framework for the Witwatersrand Basin and environs: towards a time-constrained depositional model. South African Journal of Geology 94 (1), 86–95.
Robb, L.J., Meyer, F.M., 1995. The Witwatersrand Basin, South Africa: geological framework and mineralization processes. Ore Geology Reviews 10 (2), 67–94.
Shannon, R.D., 1976. Revised effective ionic radii and systematic studies of interatomic distances in halides and chalcogenides. Acta Crystallographica Section A Crystal Physics Diffraction Theoretical and General Crystallography 32 (5), 751–767.
Stacey, J.t., Kramers, J., 1975. Approximation of terrestrial lead isotope evolution by a two-stage model. Earth and Planetary Science Letters 26 (2), 207–221.
Thompson, K., Lawrence, D., Larson, D., Olson, J., Kelly, T., Gorman, B., 2007. In situ site-specific specimen preparation for atom probe tomography. Ultramicroscopy 107 (2), 131–139.
Valley, J.W., Cavosie, A.J., Ushikubo, T., Reinhard, D.A., Lawrence, D.F., Larson, D.J., Clifton, P.H., Kelly, T.F., Wilde, S.A., Moser, D.E., 2014. Hadean age for a post-magma-ocean zircon confirmed by atom-probe tomography. Nature Geoscience 7 (3), 219–223.
White, L.F., Darling, J., Moser, D., Reinhard, D., Prosa, T., Bullen, D., Olsen, D., Larson, D., Lawrence, D., Martin, I., 2017. Atomic-scale age resolution of planetary events. Nature Communications 8, 1–6.
Wickham, L., Schwarz, K., Stölken, J., 1999. Rules for forest interactions between dislocations. Physical Review Letters 83 (22), 4574.
Zhou, S., Preston, D., Lomdahl, P., Beazley, D., 1998. Large-scale molecular dynamics simulations of dislocation intersection in copper. Science 279 (5356), 1525–1527.

Please cite this article in press as: Fougerouse, D., et al., Time-resolved, defect-hosted, trace element mobility in deformed Witwatersrand pyrite, Geoscience Frontiers (2018), https://doi.org/10.1016/j.gsf.2018.03.010